

Gatemon Benchmarking and Two-Qubit Operation

L. Casparis,¹ T. W. Larsen,¹ M. S. Olsen,¹ F. Kuemmeth,¹
P. Krogstrup,¹ J. Nygård,^{1,2} K. D. Petersson,¹ and C. M. Marcus¹

¹Center for Quantum Devices, Station Q Copenhagen,

Niels Bohr Institute, University of Copenhagen, Copenhagen, Denmark

²Nano-Science Center, Niels Bohr Institute, University of Copenhagen, Copenhagen, Denmark

Recent experiments have demonstrated superconducting transmon qubits with semiconductor nanowire Josephson junctions. These hybrid gatemon qubits utilize field effect tunability characteristic for semiconductors to allow complete qubit control using gate voltages, potentially a technological advantage over conventional flux-controlled transmons. Here, we present experiments with a two-qubit gatemon circuit. We characterize qubit coherence and stability and use randomized benchmarking to demonstrate single-qubit gate errors below 0.7% for all gates, including voltage-controlled Z rotations. We show coherent capacitive coupling between two gatemons and coherent swap operations. Finally, we perform a two-qubit controlled-phase gate with an estimated fidelity of 91%, demonstrating the potential of gatemon qubits for building scalable quantum processors.

PACS numbers: 03.67.Lx, 81.07.Gf, 85.25.Cp

The scalability and ubiquity of semiconductor technology make it an attractive platform for a quantum processor. Semiconductor qubit devices offer simple and flexible control using voltages on high impedance gate electrodes that readily allow low-power operation at cryogenic temperatures. However, such field effect-based control also makes semiconductor qubits susceptible to electrical charge noise that can strongly degrade the fidelity of gate operations. In both semiconductor charge qubits and spin qubits using exchange coupling, charge noise directly modulates the energy splitting between states, resulting in inhomogeneous dephasing times that are typically only ~ 10 times longer than gate operation times [1–4]. Recently a new semiconductor-based qubit, the gatemon, has been introduced [5, 6]. This hybrid qubit is a superconducting transmon qubit that, crucially, features a semiconductor Josephson junction (JJ). Gate-mons therefore combine the *in situ* tunability of a semiconductor with the simple connectivity and operation of transmons [7, 8]. Initial experiments measured microsecond dephasing times that far exceeded ~ 10 ns gate operation times [6], encouraging further investigation and optimization of this qubit.

In this Letter, we explore coherence and gate operations of gatemons in a two-qubit circuit. We study the influence of the distinct gatemon spectrum on coherence and use Ramsey interferometry to precisely probe the stability of the semiconductor JJ. The excellent stability observed together with improved coherence allow for randomized benchmarking of single-qubit gates [9, 10], including Z-rotations implemented with gate pulses [11, 12]. We also demonstrate coherent capacitive coupling between two gatemons and coherent swap oscillations. Finally, with the implementation of a controlled-phase gate, we demonstrate that semiconductor-based gatemons are conceptually similar to transmons, but with the technological advantage of

full voltage control, making them ideally suited for large-scale quantum processors.

Figure 1(a) shows the two-qubit device. As with conventional transmons, each gatemon operates as an LC oscillator with a nonlinear inductance due to the JJ. This

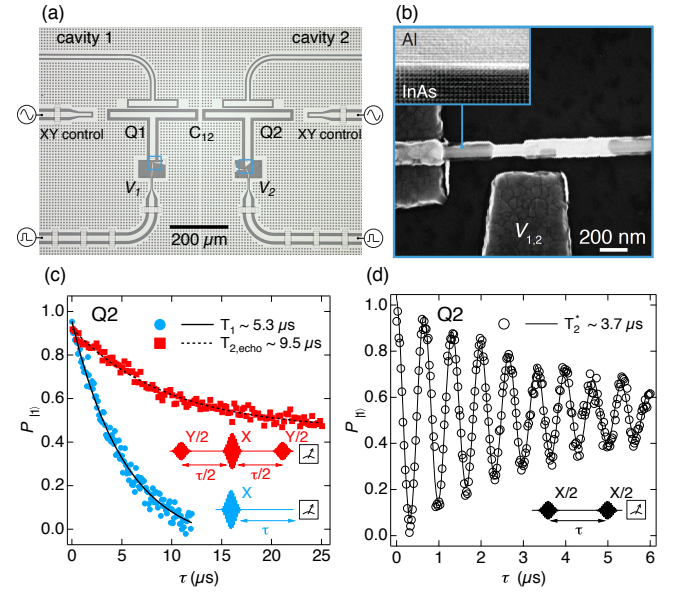


FIG. 1. Two-qubit device and single gatemon quantum coherence. (a) Optical micrograph of the two gatemon device. Each qubit consists of a T-shaped island and a gated Al-InAs-Al Josephson junction. (b) Scanning electron micrograph of the gated semiconductor weak link Josephson junction of Q1. (c) Lifetime measurement for Q2 (blue) with qubit resonance frequency $f_Q = 5.225$ GHz. In red we perform an echo experiment to determine $T_{2,\text{echo}} \sim 9.5 \mu\text{s}$. The solid and dashed lines are exponential fits. Inset: pulse sequences for dephasing ($T_{2,\text{echo}}$) [red] and relaxation (T_1) [blue] measurements. (d) A Ramsey experiment is performed to determine T_2 for Q2 with the pulse sequence shown as an inset. The solid line is a fit to an exponentially damped sinusoid.

allows us to address the qubit states $|0\rangle$ and $|1\rangle$ with a transition frequency $f_Q \approx \sqrt{8E_C E_J}/h$, where E_C is the charging energy and E_J is the Josephson coupling energy [7, 13]. In the case of the gatemon, the JJ is a superconductor-semiconductor-superconductor (S-Sm-S) junction with a few-channel Sm region, allowing E_J to be tuned using a gate voltage that controls the carrier density in the Sm region.

The sample is fabricated following the recipe described in Ref. [6], but with the thermal oxide layer removed from the silicon substrate to reduce capacitor loss. The JJ is formed by selectively wet etching a segment of a ~ 30 nm thick Al shell epitaxially grown around a ~ 75 nm diameter single crystal InAs nanowire [14]. For qubit 1 (Q1) and qubit 2 (Q2) the junction lengths are 220 nm and 200 nm respectively. For each qubit, E_C/h is determined by the capacitance of the T-shaped Al island to the surrounding ground plane and designed to be ~ 200 MHz with E_J/E_C tuned to 70 – 130 using the side gate voltage $V_{1(2)}$ for Q1(2). The interqubit coupling rate g_{12} is determined by the capacitance C_{12} between the two islands. From electrostatic simulations we estimate $2g_{12}/2\pi \approx 20$ MHz for $f_Q = 6$ GHz.

Qubit manipulation is performed using phase-controlled microwave pulses for rotations around axes in the $X - Y$ plane of the Bloch sphere and voltage pulses on $V_{1,2}$ for Z -axis rotations. For readout, the two qubits are coupled to individual $\lambda/4$ superconducting cavities (with resonant frequencies $f_{C1} \sim 7.81$ GHz and $f_{C2} \sim 7.73$ GHz), both coupled to a common feed line [15]. Crossover wiring on control lines is used to tie together interrupted regions of the ground plane to help suppress spurious modes [16]. The sample is placed inside an Al box, surrounded by a cryoperm shield and mounted at the mixing chamber of a cryogen-free dilution refrigerator with base temperature < 50 mK [17].

Figure 1(c) shows a lifetime measurement for Q2. With the qubit excited to the $|1\rangle$ state with a π pulse, the delay time τ before readout is varied and the decay (blue) fitted to an exponential, giving $T_1 = 5.3 \mu\text{s}$. We attribute the factor of ~ 10 improvement in lifetime relative to Ref. [6] to improved sample shielding and reduced interface losses due to the removal of the lossy thermal SiO_2 layer [18]. T_2^* is determined by a Ramsey measurement (Fig. 1(d)), where two $X/2$ pulses are separated by delay time τ [19]. A fit to the decay of the Ramsey fringes gives a dephasing time $T_2^* = 3.7 \mu\text{s}$, comparable to dephasing times for flux-controlled transmon devices [20]. We perform an echo experiment by inserting a refocussing X pulse between two $Y/2$ pulses (Fig. 1(c), red). The extracted $T_{2,\text{echo}} = 9.5 \mu\text{s} \approx 2T_1$ indicates that gatemon dephasing is dominated by low frequency noise [21].

In present devices, the gatemon spectrum is a non-monotonic function of gate voltage, reflecting the effect of mesoscopic fluctuations in the transmission through the nanowire [5, 6, 22]. In Fig. 2 we examine how this

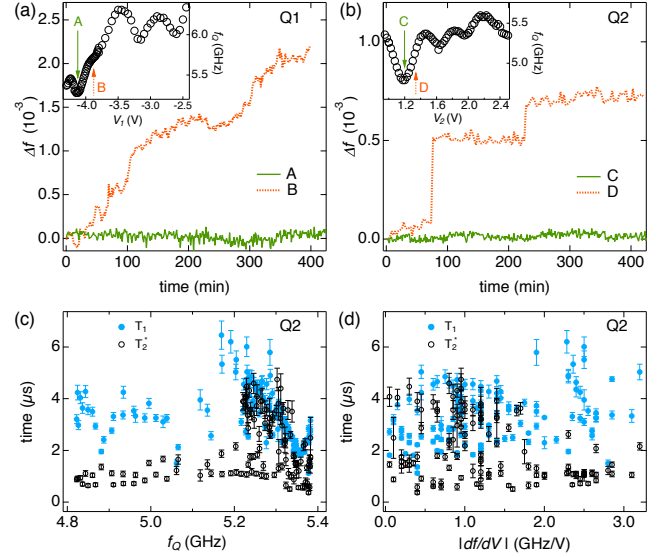


FIG. 2. Qubit spectroscopy and qubit frequency drift. (a), (b) The insets show the resonance frequency f_Q of Q1 (Q2) as a function of gate voltage V_1 (V_2). We identify sweet spots A (C) and non sweet spots B (D) in the qubit spectra. The main panels plot the normalized change in qubit resonance frequency, Δf of Q1 (Q2) as a function of time, measured at points A (C) (green, solid line) and at B (D) (orange, dashed line). (c) T_1 (solid symbols, blue) and T_2^* (empty symbols, black) of Q2 as a function of f_Q . The error bars indicate the variance of several consecutive measurements. The corresponding gate voltage range is $V_2 = 1$ V–2 V. (d) Lifetimes and coherence times plotted against the derivative of the frequency with respect to gate voltage, $|df/dV|$.

non-monotonic response impacts the stability of f_Q , T_1 and T_2^* . Insets of Figs. 2(a) and (b) plot the qubit transition frequency as a function of gate voltage, as determined by sweeping the XY qubit microwave drive at each gate voltage. Points A and C in Figs. 2(a) and (b) insets are so-called sweet spots where the spectrum is to first order insensitive to gate voltage fluctuations. At these operating points, the drift of the resonance frequencies $\Delta f(t) = (f_Q(t) - f_Q(0))/f_Q(0)$ as measured with a Ramsey experiment, is very small over several hours. The frequency drift has a standard deviation of 55 and 15 parts per million for Q1 and Q2 respectively [Fig. 2(a) and (b) main panels, green solid curves]. Away from sweet spots [Figs. 2(a) and (b) main panels, dashed orange curves], we observe two distinct types of behavior. Q1 drifts slowly on a timescale of hours, whereas Q2 exhibits discrete jumps in f_Q . The slow timescales of these drifts allow for reproducible T_1 (blue) and T_2^* (black) measurements for Q2 [Fig. 2(c)]. Coherence times are on the order of μs but widely fluctuating, similar to observations for flux-controlled transmons [15]. The region of short coherence at ~ 5.35 GHz could be due to coupling to a two level system [20]. No correlations between sweet spots and coherence times are observed, when plot-

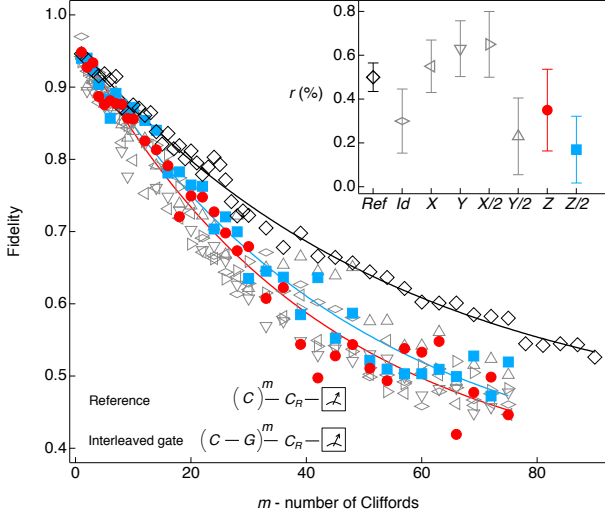


FIG. 3. Randomized benchmarking of single-qubit gates. The upper right inset serves as a legend and plots the extracted gate errors r for the reference, microwave gates and the Z rotations. We apply m single-qubit Clifford gates C to Q2. The Clifford gates are all generated by one or more Gaussian shaped microwave pulses of length 28 ns ($\sigma = 7$ ns). The lower left inset shows the two random sequence types applied to determine the gate error r . Both the random reference and interleaved gate G sequences are followed by a recovery pulse C_R , and a measurement. The main panel plots the averaged fidelity over many different random sequences for all gates investigated. The reference is shown in black. Interleaved gates benchmarked include microwave pulses (grey) and the gate pulsed Z rotations Z (red) and $Z/2$ (blue), solid lines are fits to a power law.

ting the data as a function of the derivative $|df/dV|$ of the spectrum [Fig. 2(d)]. In the remaining experiments, gatemon operation is restricted to sweet spots, e.g. A (C) for Q1 (Q2) unless noted. Away from such sweet spots, the slow timescale of the observed drift suggests it could be readily stabilized using feedback in future experiments [23].

The fidelity of single-qubit gates is an important figure of merit for establishing the feasibility of a qubit platform for quantum computation. We use randomized benchmarking with Clifford gates to evaluate the single-qubit gate fidelity for Q2 [10]. The Clifford gates are all generated by one or more Gaussian shaped microwave pulses, each taking $t_{\text{gate}} = 28$ ns (standard deviation, $\sigma = 7$ ns). The microwave pulses are tuned up using both the AllXY pulse sequence [24] and randomized sequences [25]. To benchmark the average error per Clifford, a random gate sequence of length m is applied, followed by a recovery pulse C_R projecting the random state back into the ground state and a measurement. The ground state population serves as a measure of sequence fidelity, which decays with increasing m [Fig. 3, black open symbol]. Fitting the decay with the functional form $Ap^m + B$ yields the average fidelity p per Clifford gate. From a best fit

[Fig. 3, solid black] we find the reference average fidelity $p_{\text{ref}} = 0.98$. Parameters $A = 0.53$ and $B = 0.42$ quantify state preparation and measurement errors. As only microwave pulses are used to generate the whole single-qubit Clifford set, an average Clifford gate consists of 1.875 single pulses [11]. We extract the average single-qubit gate error $r_{\text{ref}} = (1 - p_{\text{ref}})/(2 \cdot 1.875) = 0.5 \pm 0.07\%$.

To benchmark individual gates, a specific gate G is interleaved with a random Clifford m times [10], followed by a C_R gate and readout [Fig. 3 lower left inset]. A fit to the decay gives p_G . Using the average Clifford gate fidelity as reference, we extract the specific gate error $r_G = (1 - p_G/p_{\text{ref}})/2$. Figure 3 shows all benchmarked microwave gates in grey, including the identity operation Id . The inset displays the extracted errors for different gates, which are consistent with the average microwave gate error. Unique to the gatemon implementation of the transmon are rotations around the Z-axis performed by applying a voltage pulse. The voltage pulses are nominally square pulses with length 28 ns with amplitude optimized using random sequences with $m \geq 10$ [25]. Benchmarking $Z/2$ and Z rotations, the fidelity decays of both gates are found to be indistinguishable from microwave gates, with extracted errors of $r_Z = 0.35 \pm 0.19\%$ and $r_{Z/2} = 0.18 \pm 0.15\%$ [Fig. 3]. With $T_1 = 3.5 \mu\text{s}$ at point C, all gate errors [Fig. 3 inset] are close to the limit set by relaxation, $r_{\text{limit}} = t_{\text{gate}}/3T_1 = 0.3\%$ [26].

To probe the two-qubit coupling, we measure the spectrum while tuning Q1 and Q2 into resonance, driving both qubits through the same XY control line. On resonance, the two-qubit states hybridize due to the capacitive coupling C_{12} and an anticrossing is observed, see Fig. 4(a). We note the disappearance of the lower branch upon hybridizing, a signature of dark and a bright state formation [27].

Applying the pulse sequence in Fig. 4(b), a single excitation can coherently oscillate between Q1 and Q2. With the two qubits detuned by ~ 200 MHz and Q1 idling, Q2 is prepared in $|1\rangle$ away from the resonance and then a gate pulse is applied for time τ , to bring Q2 into resonance with Q1 [28]. Depending on τ and the pulse amplitude ΔV_2 , elementary excitations swap between the two qubits, creating single excitation superpositions of the two qubits. Figure 4(c) shows the typical chevron pattern of swap oscillations [29]. Figure 4(d) shows the swap oscillations for both Q1 and Q2 idling at A and C. From the frequency of sine fits to the oscillations (solid lines), we extract the interaction rate $2g_{12}/2\pi = 17.8$ MHz.

Due to the negative anharmonicity of gatemon qubits, the $|20\rangle$ - $|11\rangle$ anticrossing is used to implement a controlled-phase gate following Ref. [30]. Figure 5(a) illustrates the c_Z^π tune-up procedure. Q1 serves as a control qubit and is either prepared in $|0\rangle$ (blue) or $|1\rangle$ (red). To measure the phase acquired by the target qubit, Q2 is prepared in the $(|0\rangle + |1\rangle)/\sqrt{2}$ state. By applying a gate

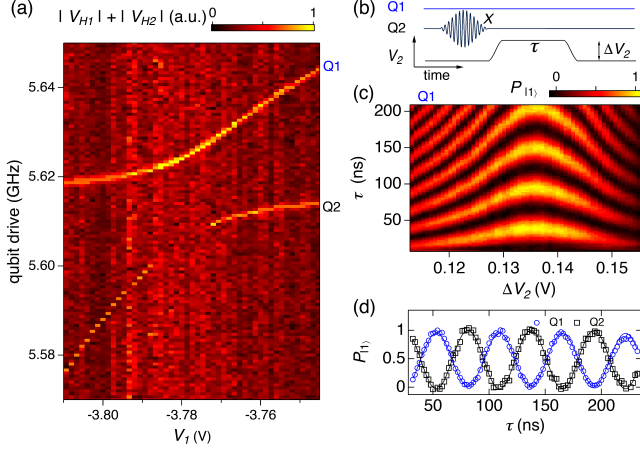


FIG. 4. Coherent gatemon coupling. (a) Measurement of the avoided level crossing between Q1 and Q2. The sum of the normalized heterodyne readout amplitude $|V_{H1}| + |V_{H2}|$ for both qubits is shown as a function of the qubit drive and V_1 ($V_2 = 2.25$ V). On resonance at $V_1 = -3.78$ V the lower branch disappears, suggesting the formation of a dark state. (b) Pulse sequence to probe the coherent coupling between the qubits. With Q1 and Q2 detuned, Q1 is prepared in the ground state and an X pulse prepares Q2 in $|1\rangle$. A gate pulse with amplitude ΔV_2 is turned on for a time τ and brings Q2 close to or in resonance with Q1. The flanks of the gate pulse are Gaussian with $\sigma = 4$ ns. (c) The $|1\rangle$ state probability, P_{11} , for Q1 as a function of ΔV_2 and τ . (d) P_{11} for both Q1 and Q2 at the voltage pulse amplitude that brings the two qubits into resonance. The flanks of the gate pulse are elongated to $\sigma = 8$ ns, to account for the larger detuning relative to (c).

pulse on V_2 , the system is brought close to the $|20\rangle$ - $|11\rangle$ anticrossing (schematic in the inset of Fig. 5(b)). For Q1 in $|0\rangle$ (grey dashed line) Q2 only acquires a dynamical phase due to the change in frequency, identical to a rotation around the Z -axis. For Q1 in the $|1\rangle$ state (black), Q2 acquires an additional two-qubit phase due to the anticrossing. After the gate pulse, Q2 is projected back onto the poles, by a $\pi/2$ pulse with varying phase θ [31]. The used gate pulse is 54 ns long and 0.16 V in amplitude, for which the acquired dynamical phase *mod* 2π is approximately 0 [blue in Fig. 5(b)]. For this gate pulse the controlled phase shift on Q2, if Q1 is in the $|1\rangle$ state (red), is $\sim \pi$ and thus constitutes a c_Z^{π} gate. The probability for Q2 to end up in the $|1\rangle$ state, $P_{Q2|1}$, oscillates as function of θ with a period of 2π , as expected.

The fidelity of the two-qubit gate was estimated by interleaving the c_Z^{π} gate with single-qubit random Clifford gates applied to the target qubit, Q2, with the control qubit, Q1, prepared randomly in either the $|0\rangle$ or $|1\rangle$ state, as shown in Fig. 5(c) [31, 32]. Q1 is returned to the $|0\rangle$ state after every c_Z^{π} gate. Because Q1 is only subject to X -rotations, the two-qubit phase can essentially be mapped as a single-qubit Z rotation. The sequence is repeated m times, followed by a recovery pulse C_R and readout of Q2. The main panel in Fig. 5(d) shows the fidelity decay with m , resulting in c_Z^{π} gate er-

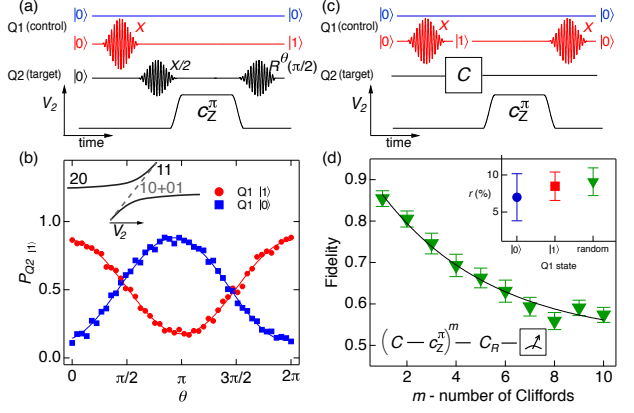


FIG. 5. Controlled-phase c_Z gate operation. (a) Pulse sequence to probe the controlled phase shift of Q2 (target). Q1 (control) is either prepared in $|0\rangle$ (blue) or $|1\rangle$ (red). The acquired single-qubit phase of Q2 is measured with a Ramsey experiment (black), where the phase of the second pulse θ is varied. Between Ramsey pulses Q2 is pulsed towards the $|20\rangle$ - $|11\rangle$ anticrossing. (b) The inset shows that independent of Q1, Q2 acquires a dynamical phase because of the change in resonance frequency (dashed line). Due to the anticrossing the target acquires an additional phase if Q1 is in the $|1\rangle$ state (solid line). In the main panel the probability of Q2 being in $|1\rangle$, $P_{Q2|1}$, is plotted as a function of θ . (c) Pulse sequence to probe the error of the c_Z^{π} gate. Q1 is prepared either in $|0\rangle$ (blue) or $|1\rangle$ (red). The c_Z^{π} gate is interleaved with a random single-qubit Clifford gate C . (d) Lower left inset: The interleaved two-qubit gate sequence is followed by a recovery pulse C_R and a measurement. The main panel shows the decay in fidelity with increasing sequence length m for a random preparation of Q1 (green). Two-qubit gate error r extracted from the decay are shown in the upper right inset for different preparations of Q1.

ror $r = 9 \pm 2\%$. If Q1 is prepared in only $|0\rangle$ or $|1\rangle$ the errors are similar (upper right inset in Fig. 5(d)). Based on measurements using an identity operation instead of a c_Z^{π} gate pulse, we estimate a 4% error due to relaxation. The remaining 5% error is coming from leakage into the $|20\rangle$ state, which can be minimized through improved pulse shaping [25, 33].

In summary, we have presented gate operations for a hybrid superconductor-semiconductor qubit, with inhomogeneous dephasing times comparable to conventional flux-controlled transmon qubits and single-qubit gate fidelities exceeding 99%. Through both optimizing gate operations and further leveraging recent advances in conventional transmon qubit lifetimes, we expect one- and two-qubit gate fidelities comparable with conventional transmons can be achieved. Combined with simple qubit control using gate voltages, gatemon qubits may present an attractive route to large scale quantum computing.

We thank John M. Martinis for helpful discussions. This work was financially supported by Microsoft Project Q, the Villum Foundation, and the Danish National Research Foundation. K.D.P. was further supported by a Marie Curie Fellowship.

-
- ated in the text with I for $\theta = \pi$ and $I/2$ for $\theta = \pi/2$.
- [1] T. Hayashi, T. Fujisawa, H. D. Cheong, Y. H. Jeong, and Y. Hirayama, Phys. Rev. Lett. **91**, 226804 (2003).
 - [2] K. D. Petersson, J. R. Petta, H. Lu, and A. C. Gossard, Phys. Rev. Lett. **105**, 246804 (2010).
 - [3] D. Kim, Z. Shi, C. B. Simmons, D. R. Ward, J. R. Prance, T. S. Koh, J. K. Gamble, D. E. Savage, M. G. Lagally, M. Friesen, S. N. Coppersmith, and M. A. Eriksson, Nature **511**, 70 (2014).
 - [4] J. R. Petta, A. Johnson, J. Taylor, E. Laird, A. Yacoby, A. Lukin, C. M. Marcus, M. Hanson, and A. C. Gossard, Science **309**, 2180 (2005).
 - [5] G. de Lange, B. van Heck, A. Bruno, D. J. van Woerkom, A. Geresdi, S. R. Plissard, E. P. A. M. Bakkers, A. R. Akhmerov, and L. DiCarlo, Phys. Rev. Lett. **115**, 127002 (2015).
 - [6] T. W. Larsen, K. D. Petersson, F. Kuemmeth, T. S. Jespersen, P. Krogstrup, J. Nygard, and C. M. Marcus, Phys. Rev. Lett. **115**, 127001 (2015).
 - [7] J. Koch, T. M. Yu, J. M. Gambetta, A. A. Houck, D. I. Schuster, J. Majer, A. Blais, M. H. Devoret, S. M. Girvin, and R. J. Schoelkopf, Phys. Rev. A **76**, 042319 (2007).
 - [8] J. A. Schreier, A. A. Houck, J. Koch, D. I. Schuster, B. R. Johnson, J. M. Chow, J. M. Gambetta, J. Majer, L. Frunzio, M. H. Devoret, S. M. Girvin, and R. J. Schoelkopf, Phys. Rev. B **77**, 180502 (2008).
 - [9] E. Knill, D. Leibfried, R. Reichle, J. Britton, R. B. Blakestad, J. D. Jost, C. Langer, R. Ozeri, S. Seidelin, and D. J. Wineland, Phys. Rev. A **77**, 012307 (2008).
 - [10] E. Magesan, J. M. Gambetta, B. R. Johnson, C. A. Ryan, J. M. Chow, S. T. Merkel, M. P. da Silva, G. A. Keefe, M. B. Rothwell, T. A. Ohki, M. B. Ketchen, and M. Steffen, Phys. Rev. Lett. **109**, 080505 (2012).
 - [11] R. Barends, J. Kelly, A. Megrant, A. Veitia, D. Sank, E. Jeffrey, T. C. White, J. Mutus, A. G. Fowler, B. Campbell, Y. Chen, Z. Chen, B. Chiaro, A. Dunsworth, C. Neill, P. J. J. O'Malley, P. Roushan, A. Vainsencher, J. Wenner, A. N. Korotkov, A. N. Cleland, and J. M. Martinis, Nature **508**, 500 (2014).
 - [12] S. Sheldon, L. S. Bishop, E. Magesan, S. Filipp, J. M. Chow, and J. M. Gambetta, arXiv preprint arXiv:1504.06597 (2015).
 - [13] J. Clarke and F. K. Wilhelm, Nature **453**, 1031 (2008).
 - [14] P. Krogstrup, N. L. B. Ziino, W. Chang, S. M. Albrecht, M. H. Madsen, E. Johnson, J. Nygård, C. M. Marcus, and T. S. Jespersen, Nat. Mater. **14**, 400 (2015).
 - [15] R. Barends, J. Kelly, A. Megrant, D. Sank, E. Jeffrey, Y. Chen, Y. Yin, B. Chiaro, J. Mutus, C. Neill, P. J. J. O'Malley, P. Roushan, J. Wenner, T. C. White, A. N. Cleland, and J. M. Martinis, Phys. Rev. Lett. **111**, 080502 (2013).
 - [16] Z. Chen, A. Megrant, J. Kelly, R. Barends, J. Bochmann, Y. Chen, B. Chiaro, A. Dunsworth, E. Jeffrey, and J. Y. Mutus, Appl. Phys. Lett. **104**, 052602 (2014).
 - [17] See the Supplemental Material at [URL to be inserted by publisher] for further details of the experimental setup.
 - [18] A. D. O'Connell, M. Ansmann, R. C. Bialczak, M. Hofheinz, N. Katz, E. Lucero, C. McKenney, M. Neeley, H. Wang, E. M. Weig, A. N. Cleland, and J. M. Martinis, Appl. Phys. Lett. **92**, 112903 (2008).
 - [19] Rotations $R_I(\theta) = e^{\pm i\sigma_I\theta/2}$ ($I = X, Y, Z$) are abbreviated in the text with I for $\theta = \pi$ and $I/2$ for $\theta = \pi/2$.
 - [20] J. Kelly, R. Barends, A. G. Fowler, A. Megrant, E. Jeffrey, T. C. White, D. Sank, J. Y. Mutus, B. Campbell, Y. Chen, Z. Chen, B. Chiaro, A. Dunsworth, I.-C. Hoi, C. Neill, P. J. J. O'Malley, C. M. Quintana, P. Roushan, A. Vainsencher, J. Wenner, A. N. Cleland, and J. M. Martinis, Nature **519**, 66 (2015).
 - [21] J. Bylander, S. Gustavsson, F. Yan, F. Yoshihara, K. Harrabi, G. Fitch, D. G. Cory, Y. Nakamura, J.-S. Tsai, and W. D. Oliver, Nat. Phys. **7**, 565 (2011).
 - [22] Y.-J. Doh, J. A. van Dam, A. L. Roest, E. P. A. M. Bakkers, L. P. Kouwenhoven, and S. De Franceschi, Science **309**, 272 (2005).
 - [23] M. D. Shulman, S. P. Harvey, J. M. Nichol, S. D. Bartlett, A. C. Doherty, V. Umansky, and A. Yacoby, Nat. Commun. **5**, 5156 (2014).
 - [24] M. Reed, *Entanglement and Quantum Error Correction with Superconducting Qubits*, Ph.D. thesis, Yale University (2013).
 - [25] J. Kelly, R. Barends, B. Campbell, Y. Chen, Z. Chen, B. Chiaro, A. Dunsworth, A. G. Fowler, I.-C. Hoi, E. Jeffrey, A. Megrant, J. Mutus, C. Neill, P. J. J. O'Malley, C. M. Quintana, P. Roushan, D. Sank, A. Vainsencher, J. Wenner, T. C. White, A. N. Cleland, and J. M. Martinis, Phys. Rev. Lett. **112**, 240504 (2014).
 - [26] P. J. J. O'Malley, J. Kelly, R. Barends, B. Campbell, Y. Chen, Z. Chen, B. Chiaro, A. Dunsworth, A. G. Fowler, I.-C. Hoi, E. Jeffrey, A. Megrant, J. Mutus, C. Neill, C. Quintana, P. Roushan, D. Sank, A. Vainsencher, J. Wenner, T. C. White, A. N. Korotkov, A. N. Cleland, and J. M. Martinis, Phys. Rev. Applied **3**, 044009 (2015).
 - [27] S. J. Srinivasan, A. J. Hoffman, J. M. Gambetta, and A. A. Houck, Phys. Rev. Lett. **106**, 083601 (2011).
 - [28] J. Majer, J. M. Chow, J. M. Gambetta, J. Koch, B. R. Johnson, J. A. Schreier, L. Frunzio, D. I. Schuster, A. A. Houck, A. Wallraff, A. Blais, M. H. Devoret, S. M. Girvin, and R. J. Schoelkopf, Nature **449**, 443 (2007).
 - [29] M. Hofheinz, H. Wang, M. Ansmann, R. C. Bialczak, E. Lucero, M. Neeley, A. D. O'Connell, D. Sank, J. Wenner, J. M. Martinis, and A. N. Cleland, Nature **459**, 546 (2009).
 - [30] L. DiCarlo, J. M. Chow, J. M. Gambetta, L. S. Bishop, B. R. Johnson, D. I. Schuster, J. Majer, A. Blais, L. Frunzio, S. M. Girvin, and R. J. Schoelkopf, Nature **460**, 240 (2009).
 - [31] Y. Chen, C. Neill, P. Roushan, N. Leung, M. Fang, R. Barends, J. Kelly, B. Campbell, Z. Chen, B. Chiaro, A. Dunsworth, E. Jeffrey, A. Megrant, J. Y. Mutus, P. J. J. O'Malley, C. M. Quintana, D. Sank, A. Vainsencher, J. Wenner, T. C. White, M. R. Geller, A. N. Cleland, and J. M. Martinis, Phys. Rev. Lett. **113**, 220502 (2014).
 - [32] J. M. Chow, J. M. Gambetta, A. D. Córcoles, S. T. Merkel, J. A. Smolin, C. Rigetti, S. Poletto, G. A. Keefe, M. B. Rothwell, J. R. Rozen, M. B. Ketchen, and M. Steffen, Phys. Rev. Lett. **109**, 060501 (2012).
 - [33] E. Lucero, M. Hofheinz, M. Ansmann, R. C. Bialczak, N. Katz, M. Neeley, A. D. O'Connell, H. Wang, A. N. Cleland, and J. M. Martinis, Phys. Rev. Lett. **100**, 247001 (2008).